

# Discrimination of breast cancer from healthy breast tissues using a three-component diffusion-weighted MRI model

Maren M. Sjaastad Andreassen<sup>1#</sup>, Ana E. Rodríguez-Soto<sup>2#</sup>, Christopher C. Conlin<sup>2</sup>, Igor Vidić<sup>6</sup>, Tyler M. Seibert<sup>2,3,4</sup>, Anne M. Wallace<sup>5</sup>, Somaye Zare<sup>6</sup>, Joshua Kuperman<sup>2</sup>, Boya Abudu<sup>7</sup>, Grace S. Ahn<sup>7</sup>, Michael Hahn<sup>2</sup>, Neil P. Jerome<sup>1,8</sup>, Agnes Østlie<sup>1</sup>, Tone F. Bathen<sup>1,9</sup>, Haydee Ojeda-Fournier<sup>2</sup>, Pål Erik Goa<sup>8,9</sup>, Rebecca Rakow-Penner<sup>2\*</sup> and Anders M. Dale<sup>2\*</sup>

<sup>1</sup>*Department of Circulation and Medical Imaging, Norwegian University of Science and Technology, Trondheim, Norway*

<sup>2</sup>*Department of Radiology, University of California, San Diego. La Jolla, CA, USA*

<sup>3</sup>*Department of Radiation Medicine and Applied Sciences, University of California, San Diego. La Jolla, CA, USA*

<sup>4</sup>*Department of Bioengineering, University of California, San Diego. La Jolla, CA, USA*

<sup>5</sup>*Department of Surgery, University of California, San Diego. La Jolla, CA, USA*

<sup>6</sup>*Department of Pathology, University of California, San Diego. La Jolla, CA, USA*

<sup>7</sup>*School of Medicine, University of California, San Diego. La Jolla, CA, USA*

<sup>8</sup>*Department of Physics, Norwegian University of Science and Technology, Trondheim, Norway*

<sup>9</sup>*Department of Radiology and Nuclear Medicine, St. Olav's University Hospital, Trondheim, Norway*

# Shared first authorship, \* Shared last authorship

## Acknowledgements/Financial support

California Breast Cancer Research Program Early Career Award, GE Healthcare, Fulbright Scholarship Program, Mid-Norway Regional Health Authority #46084400, University of California Breast Cancer Screening Program #251B-0056, NIH/NIBIB #K08EB026503.

## Corresponding author

Rebecca Rakow-Penner, M.D., Ph.D.

*Department of Radiology,*

*University of California, San Diego.*

*9452 Medical Center Dr, La Jolla, CA 92037, USA.*

*Phone: (650) 269-7132, Fax: (858) 534-1078.*

*Email: [rrakowpenner@health.ucsd.edu](mailto:rrakowpenner@health.ucsd.edu)*

## Competing Interest Statement

Dr. Dale reports that he was a Founder of and holds equity in CorTechs Labs, Inc., and serves on its Scientific Advisory Board. He is a member of the Scientific Advisory Board of Human Longevity, Inc. He receives funding through research grants from GE Healthcare to UCSD. Dr. Rakow-Penner is a consultant for Human Longevity, Inc. and receives funding through research grants from GE Healthcare. The terms of these arrangements have been reviewed by and approved by UCSD in accordance with its conflict of interest policies. Dr. Igor Vidić is employed as a consultant for Cortechs Labs, Inc. Dr. Seibert reports personal honoraria in the past three years from Varian Medical Systems, Multimodal Imaging Services Corporation, and WebMD.

## Published work

Part of the study has been accepted for presentation at ISMRM, Virtual Exhibition, 8-13. August 2020 (Andreassen MMS et al, Discrimination of breast cancer from healthy breast tissues using a tri-exponential model)

## ABSTRACT

*Purpose:* Diffusion-weighted magnetic resonance imaging (DW-MRI) is a contrast-free modality that has demonstrated ability to discriminate between pre-defined benign and malignant breast lesions. However, the ability of DW-MRI to discriminate cancer tissue from all other breast tissues in a clinical setting is unknown. Here we explore the ability to distinguish breast cancer from healthy breast tissues using signal contributions from the newly developed three-component multi-b-value DW-MRI model.

*Experimental design:* Pathology-proven breast cancer patients from two datasets ( $n=81$  and  $n=25$ ) underwent multi-b-value DW-MRI. The three-component signal contributions  $C_1$  and  $C_2$  and their product,  $C_1C_2$ , were compared to the image defined on maximum b-value ( $DWI_{\max}$ ), conventional apparent diffusion coefficient (ADC), and apparent diffusion kurtosis ( $K_{\text{app}}$ ). Ability to discriminate between cancer and healthy breast tissues was assessed by the false positive rate given sensitivity of 80% ( $FPR_{80}$ ) and receiver operating characteristic (ROC) area under the curve (AUC).

*Results:* Mean  $FPR_{80}$  for both datasets was 0.016 (95%CI=0.008-0.024) for  $C_1C_2$ , 0.136 (95%CI=0.092–0.180) for  $C_1$ , 0.068 (95%CI=0.049-0.087) for  $C_2$ , 0.159 (95%CI=0.114–0.204) for  $DWI_{\max}$ , 0.731 (95%CI=0.692–0.770) for ADC and 0.684 (95%CI=0.660-0.709) for  $K_{\text{app}}$ . Mean ROC AUC for  $C_1C_2$  was 0.984 (95%CI=0.977-0.991).

*Conclusions:* The three-component model yields a clinically useful discrimination between cancer and healthy breast tissues, superior to other DW-MRI methods and obviating pre-defining lesions by radiologists. This novel DW-MRI method may serve as non-contrast alternative to standard-of-care dynamic contrast-enhanced MRI (DCE-MRI); removing the need to administer Gadolinium contrast decreases scan time and any accumulation of Gadolinium in the brain.

## INTRODUCTION

Numerous studies have indicated that early breast cancer detection, with dynamic contrast-enhanced magnetic resonance imaging (DCE-MRI), has higher sensitivity than current screening programs (ultrasound and mammography)<sup>1-5</sup>. However, DCE-MRI has a number of limitations such as conflicting results regarding specificity<sup>2-6</sup>, dependency on expert radiologist readers, and the use of Gadolinium-based contrast agents that are linked to deposition in the brain<sup>7</sup>, additional scan time and additional costs<sup>8</sup>. In contrast, diffusion-weighted MRI (DW-MRI) does not require exogenous contrast and yields quantitative information of tissues microstructure by detecting diffusion of water molecules through application of varying degree of diffusion weighting (b-values).

Various diffusion models have demonstrated comparable ability to DCE-MRI in discriminating between *pre-defined* benign and malignant lesions in small regions of interest (ROIs) in the breast<sup>9-15</sup>. However, diffusion imaging-based tools are underexplored for discrimination of cancer tissue from all benign breast tissue (benign lesions and normal fat and fibroglandular tissue), which would increase its clinical utility and practicality in breast cancer screening, treatment evaluation, surgical planning, and surveillance, where lesions are not pre-defined by radiologists.

Multi-component modeling of the DW-MRI signal over extended ranges of b-values (typically up to 2000-3000 s/mm<sup>2</sup>) theoretically isolates the slowly diffusing water component present in cancer tissue in several organs<sup>16-20</sup>. Each component is defined by an apparent diffusion coefficient (ADC), and therefore represents a distinct pool of the water diffusion signal, with the corresponding magnitude. Vidić et al<sup>13</sup> demonstrated that the normalized magnitude of the slowest element in a two-component model was excellent (AUC=0.99) in discriminating between benign and malignant breast lesions. Further, when optimizing the multi-component model to fit the DW-

MRI signal from all breast tissues, including cancer and healthy breast tissues, the result was a three-component model with empirical ADCs determined across patients and sites<sup>21</sup>. The main objective of the current study is to explore the ability of estimates derived from a three-component model to discriminate breast cancer from healthy breast tissues and to compare it to conventional DW-MRI imaging.

## **PATIENTS AND METHODS**

### **Patients**

In order to validate the discriminatory power of the three-component model across scanners and sites, two datasets of pathology-proven breast cancer patients from a United States (US) site (n=81) and a European site (n=25) were included (Table 1). Note that 49 cases from the US site and all cases from the European site were also used to determine the three-component model with fixed ADCs for breast tissue<sup>21</sup>. In addition, cases from the European site have been previously used for DW-MRI modeling of previously defined benign and malignant lesions<sup>13,22-25</sup>, linking DW-MRI signal to histological specimen<sup>26</sup> and distortion correction techniques<sup>27</sup>.

### US site

Patients with pathology-proven breast cancer with no cytotoxic regimens, chemotherapy, or ipsilateral radiation therapy for this malignancy prior to MRI scanning were eligible for this prospective study. The study was approved by the Institutional Review Board of the US site. The recruitment of patients began in December 2015 and ended in June 2019. Tumor categorization was done by histopathologic analysis of core needle and open incisional biopsies. In total, 14 patients were excluded from the study; nine patients had contralateral cancer or mastectomy, one patient had no visible cancerous tissue on DW-MRI, and in four patients image quality was low

(low signal-to-noise ratio (n=2), poor fat saturation (n=1), and severe image distortion (n=1)), resulting in 81 patients.

### European site

This prospective study was approved by the Regional Committees for Medical and Health Research Ethics (REC Central Norway, 2011/568). The recruitment of patients began in August 2014 and ended in August 2016. Inclusion criteria and tumor categorization were similar to those of the US site; for more details, see inclusion of malignant lesions from Vidić et al<sup>13</sup>.

### **MRI Acquisition**

MRI data were acquired on a 3T GE scanner (MR750, DV25-26, GE Healthcare, Milwaukee, United States) and an 8-channel breast array coil with a bilateral axial imaging plane for the US dataset, while patients from the European dataset were imaged with a 3T Siemens scanner (Skyra, VD13-E11, Siemens Healthcare, Erlangen, Germany) and a 16-channel breast array coil with a unilateral sagittal imaging plane. Differences in scanner and pulse sequence parameters across sites were used to determine that the discriminatory potential of the three-component model is robust for data collected in different scanners and pulse sequence parameters. In addition to Gadolinium DCE-MRI and T<sub>2</sub>-images, both datasets included high b-value DW-MRI acquisition:

US site protocol: Bilateral axial DW-MRI was performed using reduced field of view (FOV) echo-planar imaging (EPI) including the following parameters: spectral attenuated inversion recovery (SPAIR) fat suppression, TE=82 ms, TR=9000 ms, b-values (number of diffusion directions)=0, 500 (6), 1500 (6), and 4000 (15) s/mm<sup>2</sup>, FOV=160x320 mm<sup>2</sup>, acquisition matrix=48x96,

reconstruction matrix=128x128, voxel size=2.5x2.5x5.0 mm<sup>3</sup>, phase-encoding (PE) direction A/P, and no parallel imaging.

European site protocol: Unilateral sagittal DW- MRI was performed using Stejskal-Tanner spin-echo EPI including the following parameters: FatSat (n=15) and SPAIR (n=10) fat suppression, TE=88 ms, TR=10,600 ms (n=15) and 11,800 ms (n=10), b-values (number of diffusion directions)=0, 200 (6), 600 (6), 1200 (6), 1800 (6), 2400 (6), and 3000 (6) s/mm<sup>2</sup>, FOV=180x180 mm<sup>2</sup>, acquisition matrix=90x90, reconstruction matrix=90x90, voxel size=2.0x2.0x2.5 mm<sup>3</sup>, PE direction A/P, generalized auto-calibrating partially parallel acquisition (GRAPPA) with acceleration factor of 2 and 24 reference lines.

## **Image Processing and Analysis**

Data were normalized to the 98th percentile of intensity within the b=0 s/mm<sup>2</sup> image, indicated by the normalization factor (N). This was done to address different image intensity scaling while simultaneously preserving contribution of T<sub>2</sub>-decay to DW-MRI signal. Noise correction<sup>28</sup> was performed to account for decreasing signal to noise ratio with increasing b-value. The observed signal (SI<sub>obs</sub>) is the mean signal across diffusion directions from one individual b-value image. Background voxels were selected by manually placing a ROI in an area in the air outside the breast on the highest b-value image, yielding the mean background intensity (SI<sub>bkg</sub>). The corrected signal intensity (SI<sub>corr</sub>) calculated from SI<sub>obs</sub> and SI<sub>bkg</sub> is given as:

$$S_{corr} = \frac{\sqrt{SI_{obs}^2 - SI_{bkg}^2}}{N} ,$$

$$S_{corr}(S_{corr} < 0) = 0$$

Furthermore, corrections for eddy current artifacts, motion<sup>17</sup> and geometric distortion<sup>29</sup> were applied for the European dataset.

Full-volume cancer and control ROIs were manually defined on DW-MRI images, guided by all available data in the exam protocol (including DCE-MRI and anatomical T<sub>2</sub>-images, Figure 1), under supervision of and validation by two breast radiologists: RRP (US site) and AØ (European site). Cancer ROIs were drawn for the lesions corresponding to pathology-proven cancer. Control ROIs were drawn for the entire contralateral breast (US site) and in a cancer-free region in the ipsilateral breast at least 10 mm away from the cancer ROI (European site), with the aim to include all representative healthy breast tissues, excluding the axillary region, large cysts (>2.5 cm), and susceptibility artifacts. Cancer and control ROIs were used to determine discriminatory performance between cancer and healthy breast tissues, respectively.

For comparison with other DW-MRI methods, the non-noise-corrected image defined on maximum b-value (DWI<sub>max</sub>), conventional apparent diffusion coefficient (ADC), and apparent diffusion kurtosis (K<sub>app</sub>) were estimated. DWI<sub>max</sub> was acquired at b=4000 s/mm<sup>2</sup> for the US dataset and b=3000 s/mm<sup>2</sup> for the European dataset. The exponential decay formulas described by Jensen et al<sup>30</sup> and the corresponding b-value limits, <1000 s/mm<sup>2</sup> and <2000 s/mm<sup>2</sup>, were used for computation of ADC and K<sub>app</sub>, respectively. Note that ADC and K<sub>app</sub> were normalized by signal at b=0 per voxel to eliminate T<sub>2</sub>-dependence<sup>30</sup> rather than dividing all voxels by the same normalization factor to preserve T<sub>2</sub> information as previously described.

To ensure that regions outside of the breast were not included in analysis, control ROIs were masked using intensity thresholding and 3D connected components (US site) or manually delineated within the breast boundary (European site) and reviewed by RRP (US site) and AØ (European site) (Figure 1 and Figure 4). Additionally, all undefined values (zero and infinite) on the image defined on  $b=0$  s/mm<sup>2</sup>, ADC and  $K_{app}$  were excluded.

### Three-component modeling of DW-MRI signal

The DW-MRI signal across all available b-values was fit with a tri-exponential model where the slowest exponential had a fixed ADC of zero, yielding a three-component model with two exponentials and one constant term. The three-component model was chosen because it represents the best fit across all voxels from both healthy breast tissues and cancer tissue determined across patients and sites<sup>21</sup>, given as:

$$S_{DWI}(b) = C_1 + C_2 \cdot e^{-b \cdot ADC_2} + C_3 \cdot e^{-b \cdot ADC_3},$$

where  $S_{DWI}$  is the diffusion signal in arbitrary units,  $b$  is the b-value in s/mm<sup>2</sup>, and  $C_i$  denotes the voxel-wise unit-less signal contribution of each component. The ADC values were fixed as previously reported in<sup>21</sup>:  $ADC_1=0$  mm<sup>2</sup>/s and therefore not expressed as an exponential,  $ADC_2=1.4 \times 10^{-3}$  mm<sup>2</sup>/s, and  $ADC_3=10.2 \times 10^{-9}$  mm<sup>2</sup>/s. Fixing ADCs ensures comparability of signal contributions across voxels and patients and avoids over-fitting.

The following parametric maps were estimated from the three-component model:  $C_1 C_2$ ,  $C_1$  and  $C_2$ . The parameters  $C_1$  and  $C_2$  were estimated directly from the model, while  $C_1 C_2$  is the corresponding product. The parametric map  $C_3$  was not included due to low cancer conspicuity<sup>21</sup>.

## **Discriminating performance between cancer and healthy breast tissues**

Clinical utility of the three-component derived parametric maps was assessed by comparing the discriminatory performance between cancer and healthy breast tissues ROIs of  $C_1C_2$ ,  $C_1$  and  $C_2$  maps,  $DWI_{max}$ ,  $ADC$ , and  $K_{app}$ . Because there were ~52 times more healthy breast tissue voxels than cancer voxels, performance in discriminating between cancer and healthy breast tissues was examined for all voxels by the expected false positive rate given a sensitivity of 80% ( $FPR_{80}$ ). In addition, the conventional performance measures receiver operating characteristic (ROC) area under the curve (AUC), sensitivity, specificity, and accuracy were estimated. Sensitivity, specificity, and accuracy were calculated for the threshold value providing optimal accuracy, defined as the mean sensitivity and specificity, assuming equal prevalence of cancer and healthy breast tissue voxels.  $C_1C_2$ ,  $C_1$ ,  $C_2$ ,  $DWI_{max}$ , and  $K_{app}$ <sup>10-12</sup> were assumed to have higher intensity for cancer compared to healthy breast tissues, while the opposite was assumed for  $ADC$ <sup>9</sup>.

## **RESULTS**

### **Sample**

The total number of cancer voxels and healthy tissue voxels from both datasets was 37,659 and 1,946,186, respectively.

### **Optimized three-component model parameters for discrimination ( $C_1$ , $C_2$ , and $C_1C_2$ )**

Probability density colormaps for the three-component model given  $C_1$  and  $C_2$  including all voxels across patients and datasets are plotted for cancer (cancer ROIs, Figure 1A) and healthy breast tissues (control ROIs, Figure 1B). These maps display two distinct probability density distributions for cancer and healthy breast tissues. The product  $C_1C_2$  discriminates cancer from healthy breast

tissues voxels, where voxels low on one or two dimensions corresponds to healthy breast tissues voxels, while cancer probability increases with increased magnitude on  $C_1$  and  $C_2$ .

The relationship between  $C_1$  and  $C_2$  demonstrates that voxels with high magnitude on both dimensions had the highest probability of cancer (Figure 1A); representative cases are given in Figure 1, and all cases are given in Supplementary Figure 1-106. Discrimination performance varied depending on healthy tissue composition in relation to the magnitude of  $C_1$  and  $C_2$  in cancer tissue.  $FPR_{80}$  was higher (indicating more false positive voxels) for  $C_1$  and  $DWI_{max}$  in a case with abundant fibroglandular tissue and high  $C_1$ -magnitude of corresponding cancer tissue (Figure 1B), compared to abundant suppressed fat tissue and high  $C_2$ -magnitude of corresponding cancer (Figure 1C). The opposite was seen for  $C_2$ , while  $C_1C_2$  suppressed both fibroglandular and fatty tissue. This shows that the  $C_1C_2$  parameter derived from the three-component model provided the optimal discrimination performance between cancer and healthy breast tissues.

### **Discriminatory performance of $C_1C_2$ compared to other DW-MRI methods**

Mean  $FPR_{80}$  for both datasets was 0.016 (95%CI=0.008-0.024) for  $C_1C_2$ , 0.136 (95%CI=0.092–0.180) for  $C_1$ , 0.068 (95%CI=0.049-0.087) for  $C_2$ , 0.159 (95%CI=0.114–0.204) for  $DWI_{max}$ , 0.731 (95%CI=0.692–0.770) for ADC and 0.684 (95%CI=0.660-0.709) for  $K_{app}$  (Figure 3).  $C_1C_2$  achieved the lowest  $FPR_{80}$  with a mean ROC AUC of 0.984 (95%CI=0.977-0.991) when compared to conventional DW-MRI; see Supplementary Table 1 for all conventional performance measures.

$C_1C_2$  had excellent performance compared to ADC and  $K_{app}$  in a wide range of representative cases (Figure 4).  $DWI_{max}$  performs well in several cases (Figure 4A-B) but underperforms compared to  $C_1C_2$ , overall (Figure 3) and particularly in a case with abundant fatty tissue (Figure 4C). In addition,  $C_1C_2$  visually improves poor DCE-MRI specificity in a case with marked background parenchymal enhancement (Figure 4D). However,  $C_1C_2$  underperforms in

cases with sparse signal from cancer tissue, such as case of non-mass enhancement (NME) DCIS (Figure 4E). In this case, all DW-MRI derived maps failed to identify tumor tissue compared to healthy breast tissues. Furthermore, there was high diffusion signal from some healthy tissue components such as cysts (Figure 5B), subareolar ducts (Figure 5A), and partial-volume artifact from the interface of fibroglandular and fatty tissue (Figure 4D, Figure 5C). High diffusion signal from cysts and ducts may be defined as non-suspicious with the assistance of  $T_2$ -images (Figure 5A-B).

## DISCUSSION

Our study shows that breast cancer can be noninvasively discriminated from healthy breast tissues using the derived parameter  $C_1C_2$  based on an advanced DW-MRI model, with results comparable to cancer detection using DCE-MRI<sup>2-6</sup> ( $FPR_{80}$  mean=0.016, 95%CI=0.008-0.024 and ROC AUC mean=0.984, 95%CI=0.977-0.991). This means the  $C_1C_2$  approach achieved very low false positive rates while detecting 80% or more of the defined cancer voxels. The discriminatory power of the  $C_1C_2$  was superior to that of independent signal contributions, conventional DW-MRI-estimates (ADC) and other methods, including kurtosis ( $K_{app}$ ) and  $DWI_{max}$ . The  $C_1C_2$  approach was performed across two different sites, scanners, and acquisition protocols, suggesting potential for real-world applications. The development of this advanced DW-MRI method allows for improved conspicuity of breast cancer relative to background breast tissue. This lays the foundation for a quantitative framework specific to pathology which may serve as an alternative to DCE-MRI.

The high discriminatory performance is due to the novel  $C_1C_2$  approach. In addition to malignancy, individual signal contributions from the three-component model were sensitive to the two primary components of healthy breast tissues: fat ( $C_1$ ) and fibroglandular ( $C_2$ ) tissue. Neither

component was sensitive to tissues with very fast diffusion properties, such as vessels, necrosis, or edema. By combining the signal contributions of the two slowest components  $C_1$  and  $C_2$ , the majority of healthy breast tissues signal was suppressed so that the output image was predominantly sensitive to cancer compared to healthy breast tissues. While optimized for cancer discrimination, the detailed relationship between the three-component model and breast microstructure remains to be studied, as it has been demonstrated for the two-component model<sup>26</sup>.

The  $C_1C_2$  approach is performed on data acquired on extended imaging protocols (b-values up to 3000 s/mm<sup>2</sup> and 4000 s/mm<sup>2</sup>) and requires at least three separate non-zero b-values. Inclusion of higher b-values likely improves discrimination by allowing better estimates of very slow diffusion characteristic of intracellular fluid within hypercellular tumors<sup>13,16-20</sup>. Furthermore, we attribute the high discriminatory performance to the normalization method, where  $T_2$ -contribution to the DW-MRI signal was retained, though noise might also have been a partial contributor. The importance of  $T_2$  has been demonstrated in separating benign and malignant breast lesions, where the image at b=0 s/mm<sup>2</sup> yielded a relatively high AUC of 0.85<sup>13</sup>.

We hypothesize that two contributing factors to the poor performance of ADC and  $K_{app}$  include the restricted diffusion component from fat tissue and elimination of  $T_2$ -effects that add to cancer discrimination. The  $FPR_{80}$  discriminatory performance of ADC and  $K_{app}$  varied greatly across subjects; at best, performing around 0.2 in selected cases (Figure 4A), but overall do no better than chance. Conversely,  $DWI_{max}$  shares the same basic properties as  $C_1C_2$  (diffusion- and  $T_2$ -weighting) and performs noticeably better than ADC and  $K_{app}$ . However,  $DWI_{max}$  is also prone to influence from fatty tissue. The  $C_1C_2$  approach better accounts for fatty tissue, conferring a major advantage over  $DWI_{max}$  and the other DWI-estimates (Figure 4C), as approximately 50% of women have almost entirely fatty breast tissue or scattered fibroglandular tissue<sup>31</sup>.

In order for  $C_1C_2$  to be a noninvasive alternative to DCE-MRI for breast cancer detection, it must have comparable or better sensitivity and specificity. DW-MRI is known to improve detection specificity<sup>9,32</sup>, which is beneficial as lesion-level DCE-MRI specificity have been reported to range from 72-97%<sup>2-6</sup>. In our study, performance was assessed per voxel, and the patient cohort was heterogenous, consisting of a large range of tumor volumes (mean=10.6 cm<sup>3</sup>, range=0.2–105.9 cm<sup>3</sup>), not reflecting the typical patient pool in the screening or surveillance setting which typically have smaller lesions. However, the high performance of discriminating cancer from all other breast tissues in comparison to other DW-MRI-based methods is highly promising and suggests clinical utility comparable to DCE-MRI.  $C_1C_2$  may be particularly useful when DCE-MRI demonstrates false positive<sup>33</sup> and false negative<sup>34</sup> interpretations in patients with moderate and marked background parenchymal enhancement (Figure 4D). Ideally,  $C_1C_2$  may assist in a non-contrast workflow with T<sub>1</sub>- and/or T<sub>2</sub>-sequences as an alternative to DCE-MRI, where false positive findings can be defined as non-suspicious with the assistance of T<sub>2</sub>-images (Figure 5A-B). Thus, successful analysis using  $C_1C_2$  removes the need to administer Gadolinium contrast, decreasing scan time and any accumulation of Gadolinium in the brain<sup>7</sup>.

Several diffusion methods aim to isolate the signal from the slowly diffusing water component from cancer tissue by utilizing broad b-value ranges<sup>10-13,16-20</sup>. Kurtosis imaging is based on a simple mathematical representation of diffusion data where the derived parameter  $K_{app}$  has proven potential utility in the breast<sup>10-12</sup>. More advanced, multi-component models with fixed ADCs have been developed to further probe the microstructure in the brain and prostate: restriction spectrum imaging (RSI, on which the  $C_1C_2$  approach is based)<sup>16,17</sup>, the VERDICT model<sup>19</sup>, and the hybrid multidimensional MRI model<sup>20</sup>. A key difference between RSI/ $C_1C_2$  and the hybrid multidimensional MRI model is that the hybrid model does not use global ADCs, making comparison across patients difficult; however, the hybrid model does incorporate multi-echo

information not available in our study. Moreover, the  $T_2$ -effects seen in  $RSI/C_1C_2$  are removed from the other two modeling approaches, potentially reducing cancer conspicuity. Although the other multi-compartment models have shown promising results as cancer biomarkers in the prostate, for example, these results may be limited in breast, where fatty tissue is an important component of healthy breast tissues.

There were some limitations to our study. First, the  $C_1C_2$  methodology did not correct for partial-volume artifacts which occurred at the interface between fatty and fibroglandular tissue (Figure 4D, Figure 5C). Such artifacts have the potential to be corrected, which was not investigated in this study but is an area of interest for future improvement. Another limitation concerned the definition of control regions; although we ensured that all control regions were verified as cancer-free, based on MRI review by an expert breast radiologist (both datasets) and exclusion of cases with pathology-proven contralateral cancer in the US dataset, we cannot know if occult cancer may have been included in the control region. The unilateral European dataset may have been particularly prone to this, as the control ROIs were defined in the same breast as the cancer (this also made the size of control regions dependent on the extent of cancer and thus variable from case to case in that dataset). Lastly, detection performance is commonly evaluated at the lesion level. This study used a voxel-wise false positive rate,  $FPR_{80}$ , as its performance measure, which does not give an absolute measure comparable to other literature. However, we argue that such a measure is useful from a radiologist's perspective, because it mimics a breast cancer examination where all voxels in the entire image are used.

In conclusion, our study is the first to demonstrate that the derived parameter  $C_1C_2$ , which is the product of the two slowest components of a three-component DW-MRI model, yields a clinically useful, noninvasive method for discrimination between cancer and healthy breast tissues. The model eliminates the need for pre-defined lesions that conventional quantitative DW-MRI

metrics use. Together with anatomical images such as  $T_2$ ,  $C_1C_2$  may assist in a combined, non-contrast workflow which could serve as an alternative to DCE-MRI. The highly promising diagnostic properties were generalized across sites, scanners, and acquisition protocols, which is important for feasibility of large-scale studies for validation in routine breast cancer detection and follow-up in comparison to DCE-MRI.

## REFERENCES:

1. Lehman CD, Blume JD, Weatherall P, et al: Screening women at high risk for breast cancer with mammography and magnetic resonance imaging. *Cancer* 103:1898-905, 2005
2. Kuhl CK, Schrading S, Leutner CC, et al: Mammography, breast ultrasound, and magnetic resonance imaging for surveillance of women at high familial risk for breast cancer. *J Clin Oncol* 23:8469-76, 2005
3. Kriege M, Brekelmans CTM, Boetes C, et al: Efficacy of MRI and mammography for breast-cancer screening in women with a familial or genetic predisposition. *The New England journal of medicine* 351:427-437, 2004
4. Leach MO, Boggis CR, Dixon AK, et al: Screening with magnetic resonance imaging and mammography of a UK population at high familial risk of breast cancer: a prospective multicentre cohort study (MARIBS). *Lancet* 365:1769-78, 2005
5. Saadatmand S, Geuzinge HA, Rutgers EJT, et al: MRI versus mammography for breast cancer screening in women with familial risk (FaMRIsc): a multicentre, randomised, controlled trial. *Lancet Oncol* 20:1136-1147, 2019
6. Peters NH, Borel Rinkes IH, Zuithoff NP, et al: Meta-analysis of MR imaging in the diagnosis of breast lesions. *Radiology* 246:116-24, 2008
7. Gulani V, Calamante F, Shellock FG, et al: Gadolinium deposition in the brain: summary of evidence and recommendations. *Lancet Neurol* 16:564-570, 2017
8. U.S. Centers for Medicare & Medicaid Services: Physician Fee Schedule Search. <https://www.cms.gov/apps/physician-fee-schedule/search/search-results.aspx?Y=0&T=0&HT=0&CT=1&H1=77049&C=1&M=5>, Published January 11, 2019. Accessed December 26, 2019
9. Chen X, Li WL, Zhang YL, et al: Meta-analysis of quantitative diffusion-weighted MR imaging in the differential diagnosis of breast lesions. *BMC Cancer* 10:693, 2010
10. Nogueira L, Brandao S, Matos E, et al: Application of the diffusion kurtosis model for the study of breast lesions. *Eur Radiol* 24:1197-203, 2014
11. Wu D, Li G, Zhang J, et al: Characterization of breast tumors using diffusion kurtosis imaging (DKI). *PLoS One* 9:e113240, 2014
12. Christou A, Ghiatas A, Priovolos D, et al: Accuracy of diffusion kurtosis imaging in characterization of breast lesions. *Br J Radiol* 90:20160873, 2017
13. Vidic I, Egnell L, Jerome NP, et al: Modeling the diffusion-weighted imaging signal for breast lesions in the  $b = 200$  to  $3000$  s/mm<sup>2</sup> range: quality of fit and classification accuracy for different representations. *Magn Reson Med*, 2020
14. Luo J, Hippe DS, Rahbar H, et al: Diffusion tensor imaging for characterizing tumor microstructure and improving diagnostic performance on breast MRI: a prospective observational study. *Breast Cancer Res* 21:102, 2019
15. Iima M, Kataoka M, Kanao S, et al: Intravoxel Incoherent Motion and Quantitative Non-Gaussian Diffusion MR Imaging: Evaluation of the Diagnostic and Prognostic Value of Several Markers of Malignant and Benign Breast Lesions. *Radiology* 287:432-441, 2018
16. Rakow-Penner RA, White NS, Parsons JK, et al: Novel technique for characterizing prostate cancer utilizing MRI restriction spectrum imaging: proof of principle and

initial clinical experience with extraprostatic extension. *Prostate Cancer Prostatic Dis* 18:81-5, 2015

17. White NS, McDonald CR, Farid N, et al: Diffusion-weighted imaging in cancer: Physical foundations and applications of restriction spectrum imaging. *Cancer Research* 74:4638-4652, 2014
18. Karunamuni RA, Kuperman J, Seibert TM, et al: Relationship between kurtosis and bi-exponential characterization of high b-value diffusion-weighted imaging: application to prostate cancer. *Acta Radiologica* 59:1523-1529, 2018
19. Panagiotaki E, Chan RW, Dikaios N, et al: Microstructural characterization of normal and malignant human prostate tissue with vascular, extracellular, and restricted diffusion for cytometry in tumours magnetic resonance imaging. *Invest Radiol* 50:218-27, 2015
20. Chatterjee A, Bourne RM, Wang S, et al: Diagnosis of Prostate Cancer with Noninvasive Estimation of Prostate Tissue Composition by Using Hybrid Multidimensional MR Imaging: A Feasibility Study. *Radiology* 287:864-873, 2018
21. Rodriguez-Soto AE, Andreassen MMS, Conlin CC, et al: Characterization of the Diffusion Signal of Breast Tissues using Multi-exponential Models. medRxiv:2020.04.27.20082271, 2020
22. Vidic I, Egnell L, Jerome NP, et al: Support vector machine for breast cancer classification using diffusion-weighted MRI histogram features: Preliminary study. *J Magn Reson Imaging* 47:1205-1216, 2018
23. Teruel JR, Goa PE, Sjobakk TE, et al: Diffusion weighted imaging for the differentiation of breast tumors: From apparent diffusion coefficient to high order diffusion tensor imaging. *J Magn Reson Imaging* 43:1111-21, 2016
24. Vidic I, Jerome NP, Bathen TF, et al: Accuracy of breast cancer lesion classification using intravoxel incoherent motion diffusion-weighted imaging is improved by the inclusion of global or local prior knowledge with bayesian methods. *J Magn Reson Imaging* 50:1478-1488, 2019
25. Teruel JR, Goa PE, Sjobakk TE, et al: A Simplified Approach to Measure the Effect of the Microvasculature in Diffusion-weighted MR Imaging Applied to Breast Tumors: Preliminary Results. *Radiology* 281:373-381, 2016
26. Egnell L, Vidic I, Jerome NP, et al: Stromal Collagen Content in Breast Tumors Correlates With In Vivo Diffusion-Weighted Imaging: A Comparison of Multi b-Value DWI With Histologic Specimen From Benign and Malignant Breast Lesions. *J Magn Reson Imaging*, 2019
27. Teruel JR, Fjøsne HE, Østlie A, et al: Inhomogeneous static magnetic field-induced distortion correction applied to diffusion weighted MRI of the breast at 3T. *Magnetic Resonance in Medicine* 74:1138-1144, 2015
28. Gudbjartsson H, Patz S: The Rician distribution of noisy MRI data. *Magn Reson Med* 34:910-4, 1995
29. Holland D, Kuperman JM, Dale AM: Efficient correction of inhomogeneous static magnetic field-induced distortion in Echo Planar Imaging. *Neuroimage* 50:175-83, 2010
30. Jensen JH, Helpert JA, Ramani A, et al: Diffusional kurtosis imaging: the quantification of non-gaussian water diffusion by means of magnetic resonance imaging. *Magn Reson Med* 53:1432-40, 2005

31. American College of Radiology: Breast density: breast cancer screening. [https://www.acr.org/-/media/ACR/Files/Breast-Imaging-Resources/Breast-Density-bro\\_ACR\\_SBI.pdf](https://www.acr.org/-/media/ACR/Files/Breast-Imaging-Resources/Breast-Density-bro_ACR_SBI.pdf), Accessed March 20, 2020
32. Tsushima Y, Takahashi-Taketomi A, Endo K: Magnetic resonance (MR) differential diagnosis of breast tumors using apparent diffusion coefficient (ADC) on 1.5-T. *J Magn Reson Imaging* 30:249-55, 2009
33. Giess CS, Raza S, Birdwell RL: Patterns of nonmasslike enhancement at screening breast MR imaging of high-risk premenopausal women. *Radiographics* 33:1343-60, 2013
34. Shimauchi A, Jansen SA, Abe H, et al: Breast cancers not detected at MRI: review of false-negative lesions. *AJR Am J Roentgenol* 194:1674-9, 2010
35. Hammond MEH, Hayes DF, Wolff AC, et al: American society of clinical oncology/college of american pathologists guideline recommendations for immunohistochemical testing of estrogen and progesterone receptors in breast cancer. *Journal of oncology practice* 6:195-197, 2010
36. Wolff AC, Hammond MEH, Hicks DG, et al: Recommendations for Human Epidermal Growth Factor Receptor 2 Testing in Breast Cancer: American Society of Clinical Oncology/College of American Pathologists Clinical Practice Guideline Update. *Journal of Clinical Oncology* 31:3997-4013, 2013
37. Wolff AC, Hammond MEH, Allison KH, et al: Human Epidermal Growth Factor Receptor 2 Testing in Breast Cancer: American Society of Clinical Oncology/College of American Pathologists Clinical Practice Guideline Focused Update. *J Clin Oncol* 36:2105-2122, 2018

**Table 1.** Table of patient characteristics. ER (estrogen receptor) and PR (progesterone receptor) status were assessed by immunohistochemistry (IHC) and was considered positive if  $\geq 1\%$  stained nuclei was present in 10 high-power fields<sup>35</sup>. Human epidermal growth factor receptor 2 (HER2) status was assessed by IHC and fluorescence in situ hybridization (FISH) according to ASCO/CAP guidelines 2013<sup>36</sup> or 2018<sup>37</sup> (depending on time of recruitment); positivity was defined as an IHC score of 3+, or 2+ with a gene to chromosome ratio  $\geq 2.0$  by FISH. ER, estrogen receptor; HER2, human epidermal growth factor receptor 2; NME, non-mass enhancement; PR, progesterone receptor.

	US site	European site
No. of patients	85	25
Median patient age, years (range)	51 (20 - 84)	53 (29 – 75)
Mean tumor volume, cm <sup>3</sup> (range)	13.1 (0.2 - 105.9)	2.5 (0.5 – 5.8)
<b>Histological type</b>		
Invasive carcinoma of no special type	64	17
Invasive lobular carcinoma	6	1
Tubular carcinoma	0	1
Mucinous carcinoma	0	1
Carcinoma with medullary features	0	3
Metaplastic carcinoma of no special type	4	0
Invasive papillary carcinoma	0	1
Mixed Invasive carcinoma of no special type and Invasive lobular carcinoma	3	0
Mixed Invasive carcinoma of no special type and mucinous carcinoma	1	0
Ductal carcinoma in situ	3	1
<b>Histological grade</b>		
1	3	5
2	28	9
2/3	0	1
3	47	8
Not analyzed	3	2
<b>ER status</b>		
Positive	53	23
Negative	27	1
Not analyzed	1	1
<b>PR status</b>		
Positive	50	20
Negative	30	4
Not analyzed	1	1
<b>HER2 status</b>		
Positive	14	7
Negative	64	17
Not analyzed	3	1
<b>Lesion type mass (mass vs. NME)</b>		
Mass	67	25
NME	13	0
Mass and NME	1	0

## FIGURES

**Figure 1.** Parameter maps for  $DWI_{\max}$ ,  $C_1$ ,  $C_2$ ,  $C_1C_2$  with  $FPR_{80}$ ,  $T_2$ -images with cancer (red) and control (green) ROI overlay and probability density colormaps for cancer and control given  $C_1$  and  $C_2$  for three representative cases from the US dataset.  $FPR_{80}$  vary depending on healthy tissue composition in relation to the magnitude of  $C_1$  and  $C_2$  in cancer tissue. (A.) mixed tissue composition with cancer high on both dimensions. (B.) abundant fibroglandular tissue and high  $C_1$ -magnitude of cancer. (C.) abundant fat tissue and high  $C_2$ -magnitude of cancer.  $DWI_{\max}$  and  $C_1$  performance is poorest in (B.),  $C_2$  in (C.) while  $C_1C_2$  has perfect performance across cases. Colormaps are given on a logarithmic scale normalized to the maximum probability density value. Y- and x- axis are defined by the maximum value for each case. Grey level windows for all images are scaled to the maximum and minimum signal intensity of each case and given in arbitrary unites. Au, arbitrary unit; C, signal contribution;  $DWI_{\max}$ , image defined on maximum b-value;  $FPR_{80}$ , false positive rate given sensitivity 80%; ROI, region-of-interest.

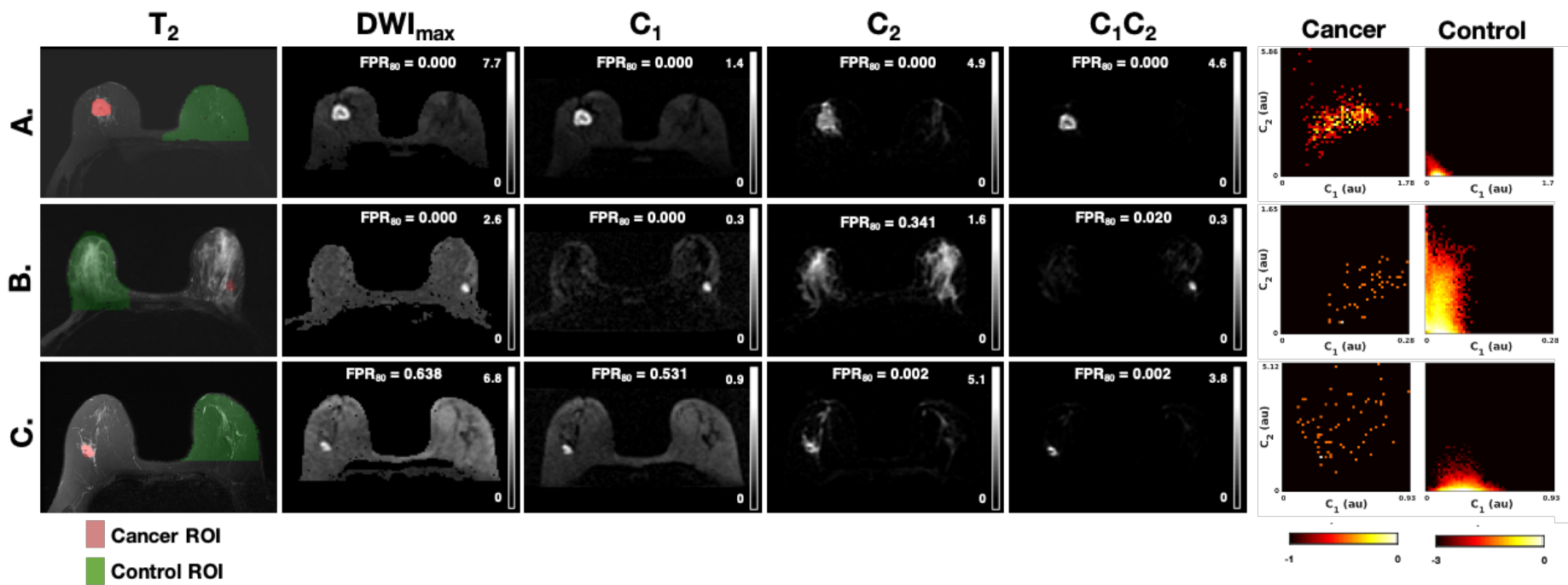


**Figure 2.** Probability density colormaps for the three-component model given  $C_1$  and  $C_2$  including all voxels across patients and datasets are given for (A.) cancer (cancer ROIs) and (B.) healthy breast tissues (control ROIs). These maps display two distinct probability density distributions for cancer and healthy breast tissues. Cancer probability increases with increased magnitude on  $C_1$  and  $C_2$ . Colormaps are given on a logarithmic scale normalized to the maximum probability density value. Au, arbitrary unit; C, signal contribution.

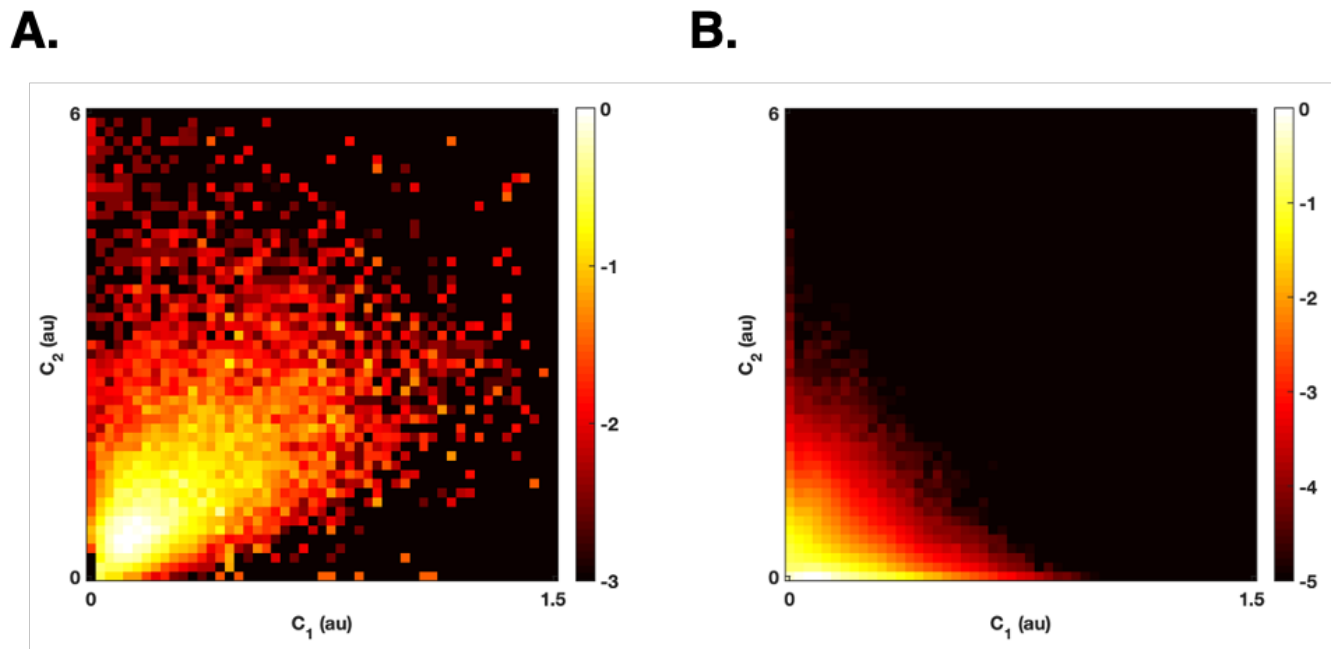


**Figure 3.** The  $FPR_{80}$  is the false positive rate given sensitivity of 80% for discriminating cancer and healthy breast tissues for three-component model parameters ( $C_1C_2$ ,  $C_1$ ,  $C_2$ ),  $DWI_{max}$ , ADC and  $K_{app}$ , given per patient across US and European dataset. Median values indicated by lines; boxes show interquartile range, block bars show data range and red crosses show outliers. The worst  $FPR_{80}$  for all maps is 0.9934, which would be 9 934 false positive voxels of one breast (one control ROI) approximated to contain 10 000 voxels ( $\sim 30$  cL). ADC; conventional apparent diffusion coefficient; C, signal contribution;  $DWI_{max}$ , image defined on maximum b-value;  $FPR_{80}$ , false positive rate given sensitivity 80%;  $K_{app}$ , apparent diffusion kurtosis.

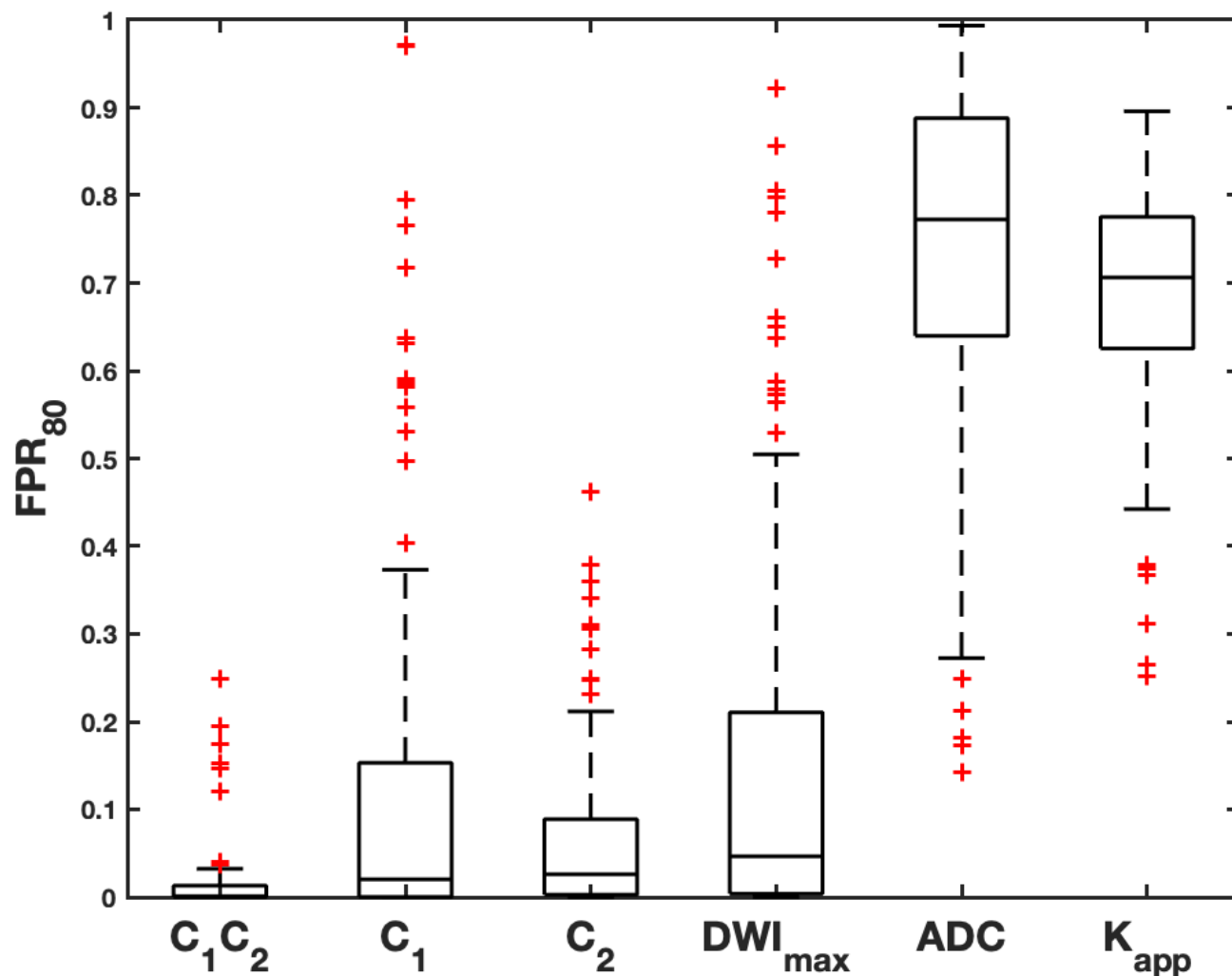


**Figure 4.**  $C_1C_2$ ,  $DWI_{max}$ , ADC and  $K_{app}$  with  $FPR_{80}$  for discrimination between cancer (red arrowhead) and healthy breast tissues (entire cancer-free contralateral breast US dataset, cancer-free ipsilateral breast European dataset) for representative cases from the US (A.-E.) and European (F.) dataset. All cases demonstrate visual similarity between DCE-MRI and  $C_1C_2$  maps with excellent performance compared to ADC and  $K_{app}$ . (A.) Excellent performance by  $C_1C_2$  and  $DWI_{max}$ . (B.) Excellent performance by  $C_1C_2$  and  $DWI_{max}$  displaying full extent of cancer involving skin. (C.) Excellent performance by  $C_1C_2$  and poor performance by  $DWI_{max}$ , ADC and  $K_{app}$  in a case with abundant fatty tissue. (D.)  $C_1C_2$  improves poor DCE-MRI specificity in a case with marked background parenchymal enhancement, but partial-volume artifact from the interface of fibroglandular and fatty tissue in the contralateral breast results in a low discriminatory performance. (E.) A case with NME DCIS where all diffusion maps fail;  $C_1C_2$  has reduced cancer signal relative to the high signal from ipsilateral sub-areolar ducts. (F.) Sagittal image plane illustrating same trends in European dataset. The worst  $FPR_{80}$  for all maps is 0.9934, which would be 9 934 false positive voxels of one breast (one control ROI) approximated to contain 10 000 voxels (~30 cL). Grey level windows for all images are scaled to the maximum and minimum signal intensity of each case. ADC; conventional apparent diffusion coefficient; Au, arbitrary unit; DCE-MRI, dynamic-contrast enhanced magnetic resonance imaging; DCIS; ductal carcinoma in situ;  $DWI_{max}$ , image defined on maximum b-value;  $FPR_{80}$ , false positive rate given sensitivity 80%;  $K_{app}$ , apparent diffusion kurtosis; NME; non-mass enhancement.

Figure 4.

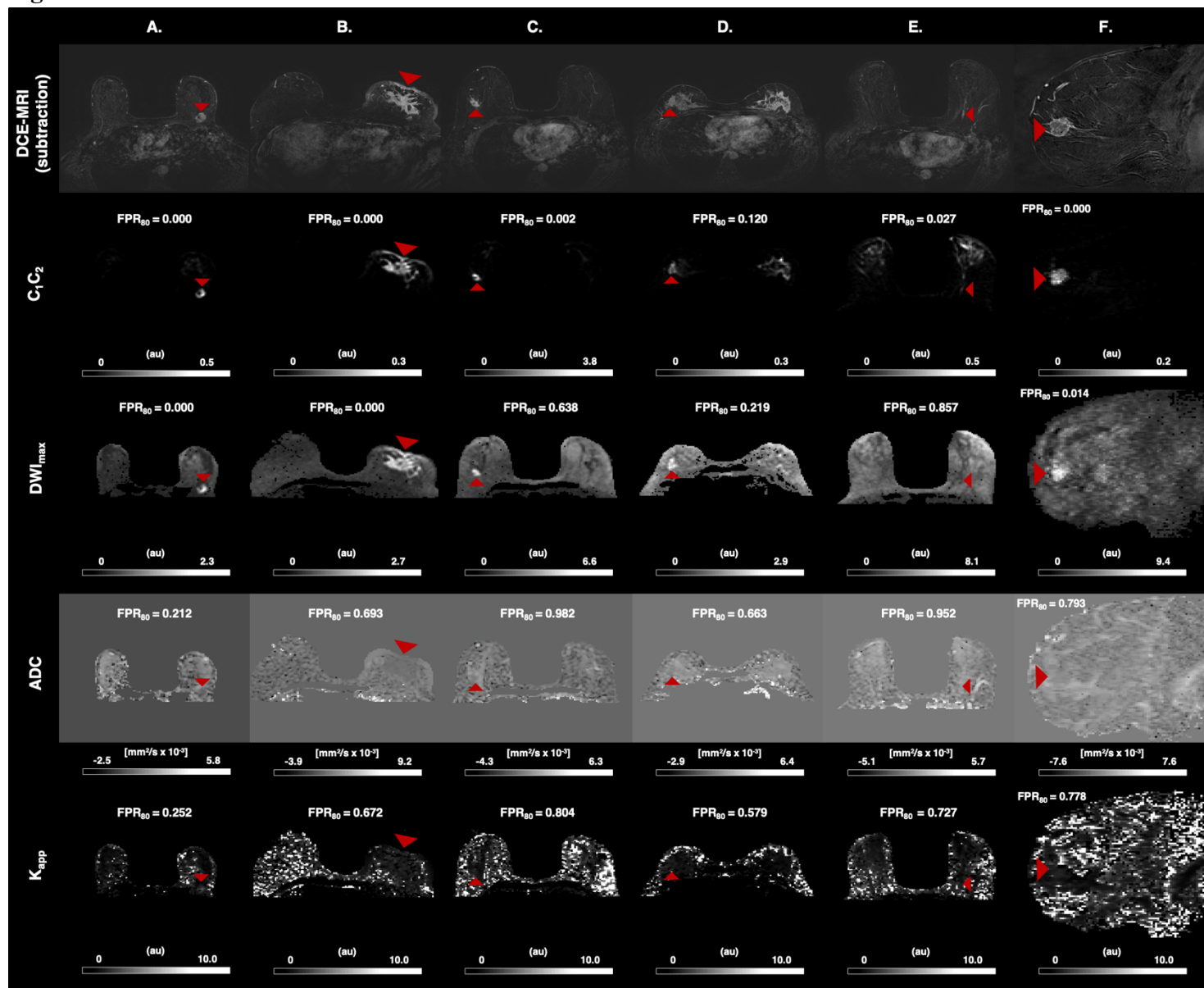


**Figure 5.** DCE-MRI and T<sub>2</sub>-images with corresponding C<sub>1</sub>C<sub>2</sub> images illustrating false positives

on C<sub>1</sub>C<sub>2</sub> (yellow arrow). (A.-B.) show that false positive lesions on C<sub>1</sub>C<sub>2</sub> can be defined as non-suspicious with the assistance of T<sub>2</sub>-images. (A.) High signal involving subareolar ducts on T<sub>2</sub>-image and C<sub>1</sub>C<sub>2</sub>, not visible on DCE-MRI. (B.) Cyst visible on T<sub>2</sub>-image and C<sub>1</sub>C<sub>2</sub>, not visible on DCE-MRI (C.) Demonstration of limitation of C<sub>1</sub>C<sub>2</sub> where background parenchymal enhancement visible on DCE-MRI and T<sub>2</sub>-image creates a partial-volume artifact corresponding to the interface between fatty and fibroglandular tissue on C<sub>1</sub>C<sub>2</sub>. Grey level windows for all C<sub>1</sub>C<sub>2</sub> images are scaled to the maximum and minimum signal intensity of each case and given in arbitrary unites. Au, arbitrary unit; C, signal contribution; DCE-MRI, dynamic-contrast enhanced magnetic resonance imaging

